Ultrasound Elastography: Efficient Estimation of Tissue Displacement Using an Affine Transformation Model

Hoda Sadat Hashemi[a], Mathieu Boily[b,c], Paul A. Martineau[b,c], and Hassan Rivaz[a,c]

[a]Department of Electrical and Computer Engineering, Concordia University, Montreal, Canada
[b]McGill University Health Centre (MUHC), Montreal, Canada
[c]PERFORM Centre, Concordia University, Montreal, Canada

ABSTRACT

Ultrasound elastography entails imaging mechanical properties of tissue and is therefore of significant clinical importance. In elastography, two frames of radio-frequency (RF) ultrasound data that are obtained while the tissue is undergoing deformation, and the time-delay estimate (TDE) between the two frames is used to infer mechanical properties of tissue. TDE is a critical step in elastography, and is challenging due to noise and signal decorrelation. This paper presents a novel and robust technique TDE using all samples of RF data simultaneously. We assume tissue deformation can be approximated by an affine transformation, and hence call our method ATME (Affine Transformation Model Elastography). The affine transformation model is utilized to obtain initial estimates of axial and lateral displacement fields. The affine transformation only has six degrees of freedom (DOF), and as such, can be efficiently estimated. A nonlinear cost function that incorporates similarity of RF data intensity and prior information of displacement continuity is formulated to fine-tune the initial affine deformation field. Optimization of this function involves searching for TDE of all samples of the RF data. The optimization problem is converted to a sparse linear system of equations, which can be solved in real-time. Results on simulation are presented for validation. We further collect RF data from *in-vivo* patellar tendon and medial collateral ligament (MCL), and show that ATME can be used to accurately track tissue displacement.

Keywords: Real-time elastography, ultrasound, time-delay estimation, TDE, Affine Transformation Prior, regularized elastography.

1. INTRODUCTION

Ultrasound elastography has evolved into many different categories such as quasi-static elastography[1] and shear-wave elastography.[2,3] In all elastography methods, a displacement field needs to be estimated between different frames of radio-frequency (RF) data. Correlation methods are common for displacement estimation, wherein RF data is divided into several blocks, and displacement of each block is calculated by maximizing cross correlation (CC) or normalized CC. A potential problem with all such approaches is that pre- and post-deformation windows can match poorly, because the data in the windows themselves may be corrupted by noise.[4,5] While the technique proposed in this work can be applied to displacement estimation for many types of elastography techniques, this work focuses on quasi-static elastography.

An alternative approach to correlation-based methods is minimization of a regularized cost function.[6,7] While discrete optimization techniques such as Dynamic Programming (DP) guarantee solving for the global optimum, they are computationally complex, and as such, are not suitable for real-time implementation. To speed such techniques, global optimization is only performed on one or few RF lines, significantly affecting robustness.[8] Previous work[9] proposed a real-time method for optimization of the cost function, but only exploited individual RF-lines at during each optimization, creating artifacts in the form of vertical streaks in the strain image. Furthermore, displacement estimation in each line depends on the initial estimate, i.e. the displacement of the previous RF-line. Hence, if there is large decorrelation in an RF-line that results in failure in its displacement estimate, the erroneous displacement propagates to the consequent RF-lines.

This paper presents a novel technique for time-delay estimation of all RF-lines simultaneously instead of utilizing individual RF-lines, thereby exploiting all the information in the entire image. We model tissue deformation using a 2D affine transformation to calculate an approximate initial displacement. We call our method

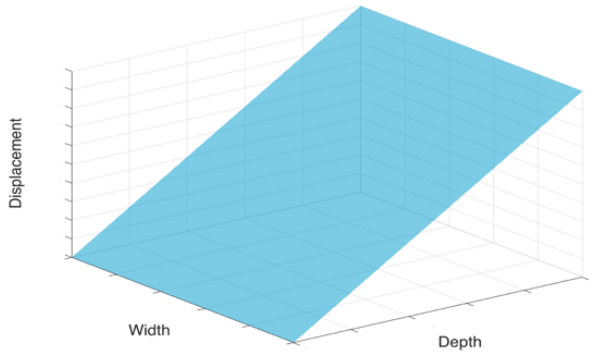

Figure 1: Displacement field between a pair of ultrasound images in a uniform tissue.

ATME: Affine Transformation Model Elastography. Since 2D affine transformation has only six degrees of freedom (DOF), it can be efficiently estimated by minimizing a quadratic error measure. Afterward, regularized global cost function is optimized by using initial displacement fields obtained from the previous step. We convert the optimization problem to a set of equations, which entails solving a sparse linear system, and as such, is computationally efficient.

The importance of the affine transformation model is twofold. First, there are only six parameters to estimate for the total RF frame, which is computationally efficient and suitable for real-time implementation. Second, the prior information that tissue deformation is relatively planar is utilized. Therefore, this method is able to estimate tissue displacements in the presence of large noise. It is also robust to signal decorrelation by exploiting the prior information that tissue deformation is smooth. This method can be applied to a range of elastography imaging techniques including freehand palpation, wherein tissue is deformed gently using a hand-held ultrasound probe.

The rest of the paper is organized as follows. We first introduce ATME, and derive the equations for estimation of TDE from RF data. We then show that ATME outperforms previous work using simulation experiments. We then collect RF data from *in-vivo* patellar tendon and medial collateral ligament (MCL) of healthy volunteers, and conclude the paper by showing that ATME can recover tendon and MCL motion in such challenging data.

2. METHODS

Let $I_1(i,j)$ and $I_2(i,j)$ be two ultrasound RF frames acquired before and after some tissue deformation, and i and j respectively be samples in the axial and lateral directions. The main idea is to enforce an affine displacement field between the two ultrasound images, such that an approximate initial displacement field can be calculated. This initial displacement field will then be utilized in a cost function that incorporates similarity of RF data intensity, as well as prior information of displacement continuity. Since the initial displacement field is affine, its estimation will be both fast and robust.

To demonstrate why an affine transformation well approximates the underlying deformation field, assume that the tissue is homogenous and isotropic. In such medium, free-hand palpation ultrasound elastography generates a planar deformation field for both axial and lateral displacements (Fig. 1). This planar deformation can be simply formulated using affine transformation, which has only 6 DOF. As such, estimation of this transformation is very efficient. Furthermore, there is a smaller chance of getting trapped in a local minimum. Real tissue is neither homogenous nor isotropic, and therefore, actual deformation is not planar. Therefore, this planar deformation can only be used as an approximation of the true underlying displacement. We use a hierarchal affine transformation model similar to the technique proposed in Ref. 10:

$$\begin{aligned} a(x,y) &= g_1 + g_2 x + g_3 y \\ l(x,y) &= g_4 + g_5 x + g_6 y \end{aligned} \tag{1}$$

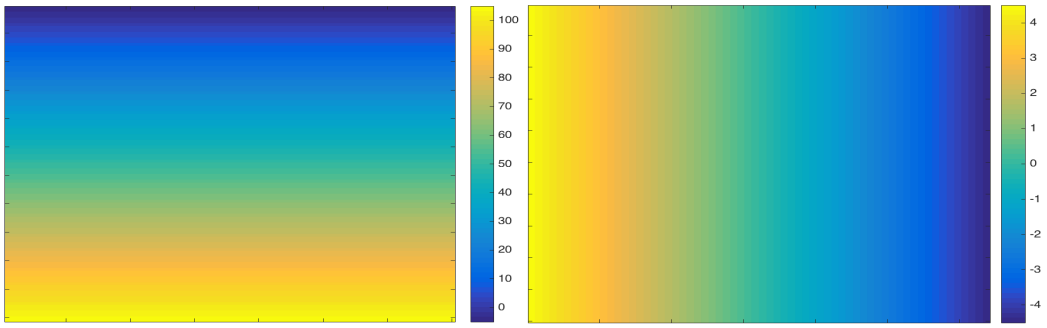

(a) Axial displacement (Ground truth) (b) Lateral Displacement (Ground truth)

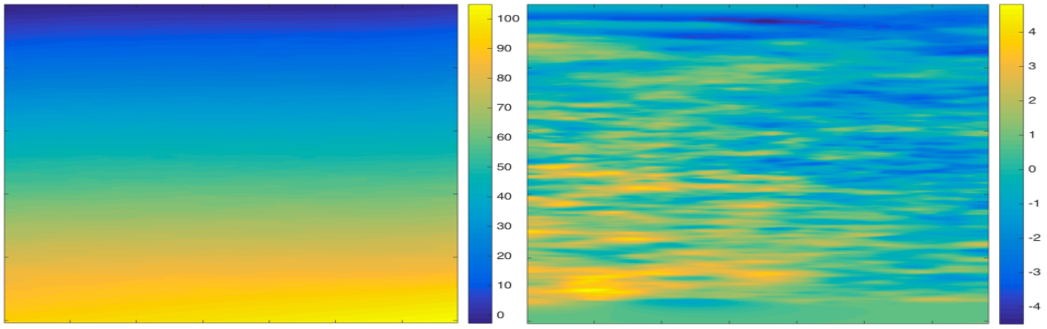

(c) Axial displacement (ATME) (d) Lateral displacement (ATME)

Figure 2: Field II and finite element simulation results. (a) and (b) show the axial and lateral ground truth displacement images of the simulation experiment. (c) and (d) are the corresponding axial and lateral displacement fields obtained from ATME.

where a and l are axial and lateral displacements of a pixel at (x, y) location. The affine parameter g_i can be obtained by minimizing an error function $E(\delta g)$ with respect to an incremental estimate g through an iterative procedure. To formulate E, let , and denote the current estimate of the affine parameter, axial and lateral displacements, respectively. The error function $E(\delta g)$ is defined as:

$$E(\delta g) = \sum_{y=1}^{n} \sum_{x=1}^{m} (\Delta I + (\nabla I)^T X \delta g)^2 \tag{2}$$

where $\Delta I = I_2(x, y) - I_1(x - a^k, y - l^k)$, and ∇I is the gradient of I_1. The matrix X is defined as:

$$D = \begin{bmatrix} 1 & x & y & 0 & 0 & 0 \\ 0 & 0 & 0 & 1 & x & y \end{bmatrix} \tag{3}$$

To simplify the notation of single pixel displacement, we simplify $a(x, y)$ to $a_{i,j}$ and $l(x, y)$ to $l_{i,j}$. Once the initial displacement field is estimated, it can be utilized in the next step. The cost function with the summation on all image pixels is defined as:

$$
\begin{aligned}
&C(\Delta a_{1,1}, \cdots, \Delta a_{m,n}, \Delta l_{1,1}, \cdots, \Delta l_{m,n}) = \\
&\sum_{j=1}^{n}\sum_{i=1}^{m}\{[I_1(i,j) - I_2(i + a_{i,j}, j + l_{i,j}) - \Delta a_{i,j} I'_{2,a} - \Delta l_{i,j} I'_{2,l}]^2 \\
&+ \alpha_1(a_{i,j} + \Delta a_{i,j} - a_{i-1,j} - \Delta a_{i-1,j})^2 + \beta_1(l_{i,j} + \Delta l_{i,j} - l_{i-1,j} - \Delta l_{i-1,j})^2 \\
&+ \alpha_2(a_{i,j} + \Delta a_{i,j} - a_{i,j-1} - \Delta a_{i,j-1})^2 + \beta_2(l_{i,j} + \Delta l_{i,j} - l_{i,j-1} - \Delta l_{i,j-1})^2\}.
\end{aligned} \tag{4}
$$

where α and β are regularization terms for axial and lateral displacements respectively. By minimizing the cost function using the initial guess $(a_{i,j}, l_{i,j})$, the sub-sample axial and lateral displacements $(\Delta a_{i,j}, \Delta l_{i,j})$ for the total image are calculated. The initial displacements $(a_{i,j}, l_{i,j})$ provided through the previous step are added to the subsample displacements. This presents us the final lateral and axial displacements i.e. $(a_{i,j} + \Delta a_{i,j}, l_{i,j} + \Delta l_{i,j})$. Once the displacement field is estimated, its spatial gradient is calculated to obtain the strain image.

3. RESULTS

We tested our proposed method on acquired data from simulation and clinical trials. In this section, we also present results of clinical trials using a previous work, DPAM,[9] to compare with ATME. Estimation of lateral displacement is significantly more difficult mainly due to the poor resolution of ultrasound images in this direction, thereby limiting previous work to only calculate axial strain images. Simultaneous estimation of the displacement filed for the entire image, however, allows us to substantially improve the quality of both axial and lateral displacements.

3.1 Simulation Experiments

Field II software[11] is used to simulate ultrasound images. The phantom is homogenous and isotropic with a Poisson ratio of $\nu = 0.49$. A uniform axial force profile is applied to the top of the phantom to generate 6% axial strain. More than 12 scatterers are randomly distributed in each cubic millimeter of the phantom to generate fully developed speckles. Further details of the data acquisition are available in Ref. 9. The Axial and lateral ground truth displacements and also the ones obtained by ATME are shown in Fig. 2. Note that the tissue is homogenous, and therefore, the deformation is assumed to be planar.

Table 1: The SNR and CNR of the strain images of Fig. 5. Maximum values are in bold font.

Experiment	SNR(DPAM)	SNR(ATME)	CNR(DPAM)	CNR(ATME)
Patellar tendon flexion (distal portion)	4.77	**10.06**	5.46	**11.98**
Patellar tendon flexion (proximal portion)	6.41	**9.17**	**3.51**	3.24
MCL pure valgus	0.7	**4.17**	1.26	**2.16**
MCL pure valgus	3.20	**6.59**	6.28	**10.70**
Average	3.77	**7.50**	4.13	**7.02**

3.2 *in-vivo* Experiments

Ethics approval was obtained at both McGill University Health Centre (MUHC) and Concordia University to collect ultrasound images of human subjects. Valgus stress was applied to the knee, and ultrasound data of the MCL was collected during the stress. In the second set of experiments, the subject freely flexed their knee, and ultrasound data was collected from the patellar tendon. Valgus stress and knee flexion generates strain in the MCL and patellar tendon respectively, and we examined whether this strain can be measured using ATME. RF data was collected with an Alpinion ultrasound machine (Bothell, WA) with an L3-12 linear transducer at the centre frequency of 11MHz and sampling frequency of 40MHz. Ligaments and tendons play a significant

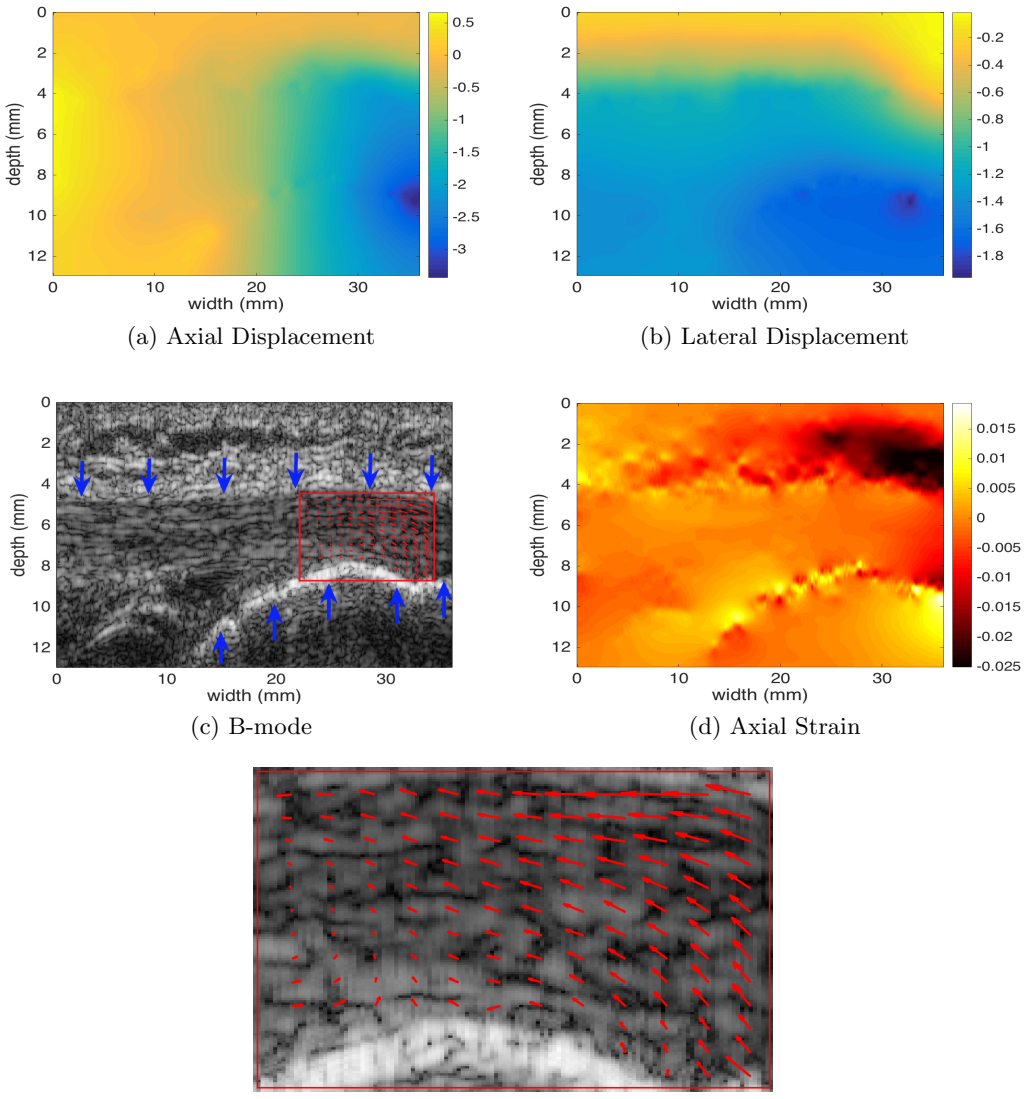

(a) Axial Displacement

(b) Lateral Displacement

(c) B-mode

(d) Axial Strain

(e) Strain directions

Figure 3: Distal tendon motion during force flexion experiment. (a) and (b) show axial and lateral displacements. (c) is the B-mode image and red arrows represent the strain directions in the tendon. (d) and (e) depict the axial strain and magnified strain directions respectively.

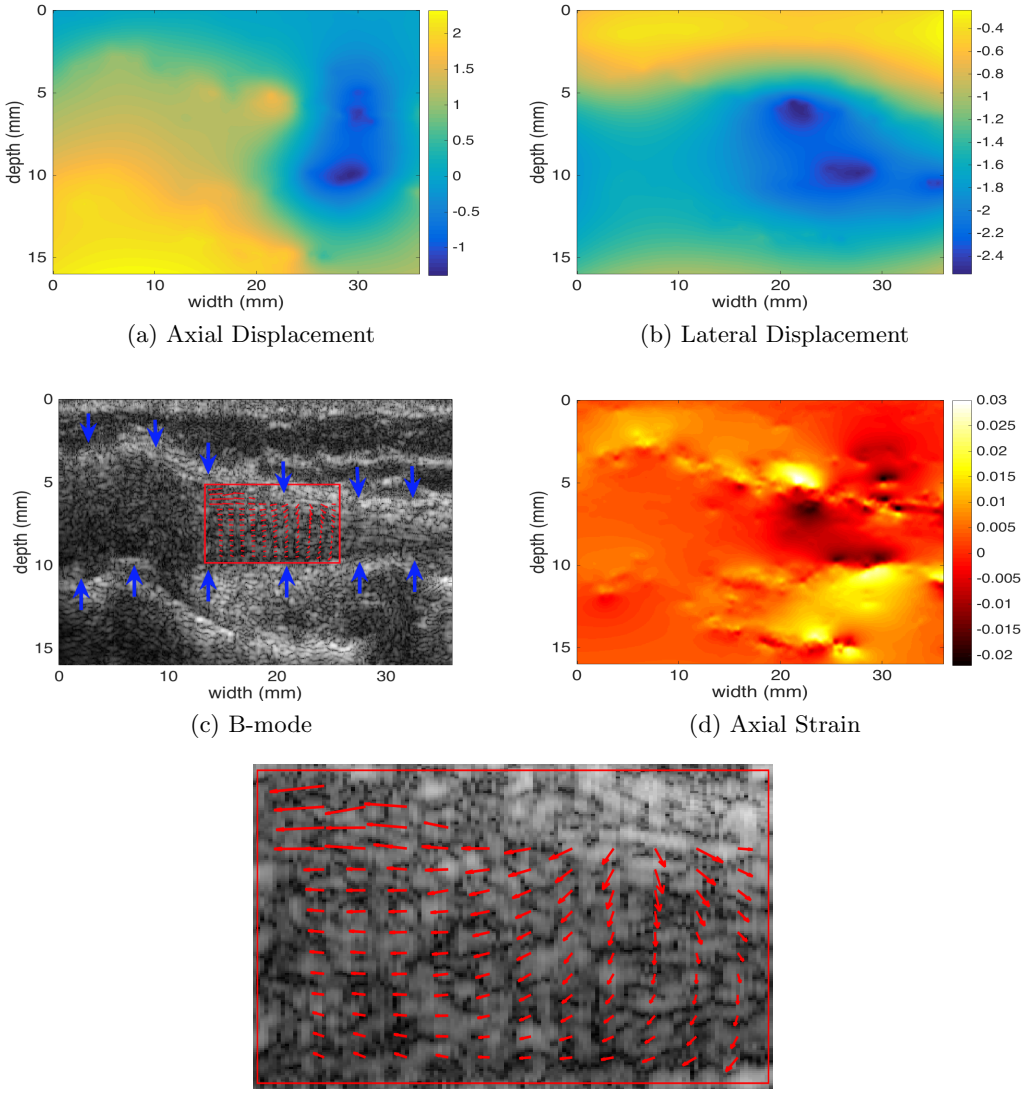

(a) Axial Displacement

(b) Lateral Displacement

(c) B-mode

(d) Axial Strain

(e) Strain directions

Figure 4: MCL during pure valgus stress experiment. (a) and (b) show axial and lateral displacements. (c) is the B-mode image and red arrows represent the strain directions in the MCL. (d) and (e) depict the axial strain and magnified strain directions respectively.

role in musculoskeletal (MSK) biomechanics, and constantly change due to factors such as aging, injury, disease or exercise. Conventional B-mode ultrasonography has been widely used as a first line diagnostic modality for superficial structures such as the patellar tendon and MCL. Strain imaging captures dynamics of tissue motion and captures deformations of the patellar tendon and MCL, which are not directly available in B-mode images. These deformation patterns reveal mechanical properties of tendon and therefore may reveal important pathology otherwise hidden in the B-mode scans.[12]

Fig. 3(a) and (b) show the displacement of the distal tendon (lower portion of patellar tendon connected to tibia) during *in-vivo* forced flexion. The B-mode image is demonstrated in (c). Red arrows represent strain directions and their relative amplitudes in a region of interest. The patellar tendon is marked with blue arrows. The axial strain is shown in (d) wherein we can clearly distinguish the boundaries of tendon from rest of the

tissue. The strain arrows in (c) are magnified and depicted in (e) for better visualization. The results in (e) are in good agreement with our expectation of strain in the patellar tendon: the strain is relatively high close to the patella (the hyperechoic dome-shaped structure in bottom left of (c) with the shadow underneath), where it is getting pulled by the joint. The strain is also tensile (arrows pointing to the left) at the top, and compressive at the bottom (arrows pointing to the right) in (e), as we expect from a bent structure (i.e. the patellar tendon).

Fig. 4(a) and (b) demonstrate the motion fields of MCL when the pure valgus stress is applied on the knee. (c) and (d) show the B-mode and strain images respectively. MCL is marked with blue arrows in (c). Strain directions which are shown with red arrows in (c) are enlarged in (e). Again, the strain field corresponds well with what we expect: high tension at the top where the extension is maximum in the bent MCL.

Fig. 5 shows B-mode images and also the strain fields calculated for the Patellar tendon and MCL during flexion. For the purposes of comparison, strain images were also calculated using a previous work, DPAM.[9] In the first row, the distal portion of the knee is shown while the forced flexion is applied to patellar tendon. In the second row, the same experiment is practiced but the proximal portion of the knee is depicted here. Third and forth rows show the MCL when pure valgus stress is placed on the knee. The valgus stress test is performed with the knee at 30° of flexion.

The unitless metrics signal to noise ratio (SNR) and contrast to noise ratio (CNR) are used to quantitatively compare the results:[1]

$$\mathrm{CNR} = \frac{C}{N} = \sqrt{\frac{2(\bar{s_b} - \bar{s_t})^2}{\sigma_b^2 + \sigma_t^2}},\ \mathrm{SNR} = \frac{\bar{s}}{\sigma} \tag{5}$$

where $\bar{s_t}$ and $\bar{s_b}$ are the spatial strain average of the target and background, and σ_t^2 and σ_b^2 are the spatial strain variance of the target and background, and $\bar{s}$ and σ are the spatial average and variance of a window in the strain image respectively. The corresponding SNR and CNR values are measured for both DPAM and ATME methods. CNR values are calculated between the target (tendon) and background (outside the target) windows each of size 50 samples × 50 samples, and are provided in Tab. 1. SNR values are also shown in the table, which are calculated for the background windows. ATME provides substantially higher SNR and CNR values compared to DPAM.

4. CONCLUSION

In this paper, we introduce a novel technique to calculate both axial and lateral displacement fields between two frames of RF data based on affine transformation prior. Optimization of the main global cost function involves solving a sparse linear system which can be solved in real time and provide the displacement field of the entire image simultaneously. We further applied strain imaging to patellar tendon and MCL, and showed that our proposed technique can be used to predict displacement and strain fields in these tissues. Future work will utilize these dynamical measurements of the patellar tendon and MCL to both improve diagnosis and manage treatment.

Acknowledgement

This work was supported by Richard and Edith Strauss Canada Foundation.

REFERENCES

[1] Ophir, J., Alam, S., Garra, B., Kallel, F., Konofagou, E., Krouskop, T., and Varghese, T., "Elastography: ultrasonic estimation and imaging of the elastic properties of tissues," *Proceedings of the Institution of Mechanical Engineers, Part H: Journal of Engineering in Medicine* **213**(3), 203–233 (1999).

[2] Parker, K. J., Doyley, M., and Rubens, D., "Imaging the elastic properties of tissue: the 20 year perspective," *Physics in medicine and biology* **56**(1), R1 (2010).

[3] Gennisson, J.-L., Deffieux, T., Fink, M., and Tanter, M., "Ultrasound elastography: principles and techniques," *Diagnostic and interventional imaging* **94**(5), 487–495 (2013).

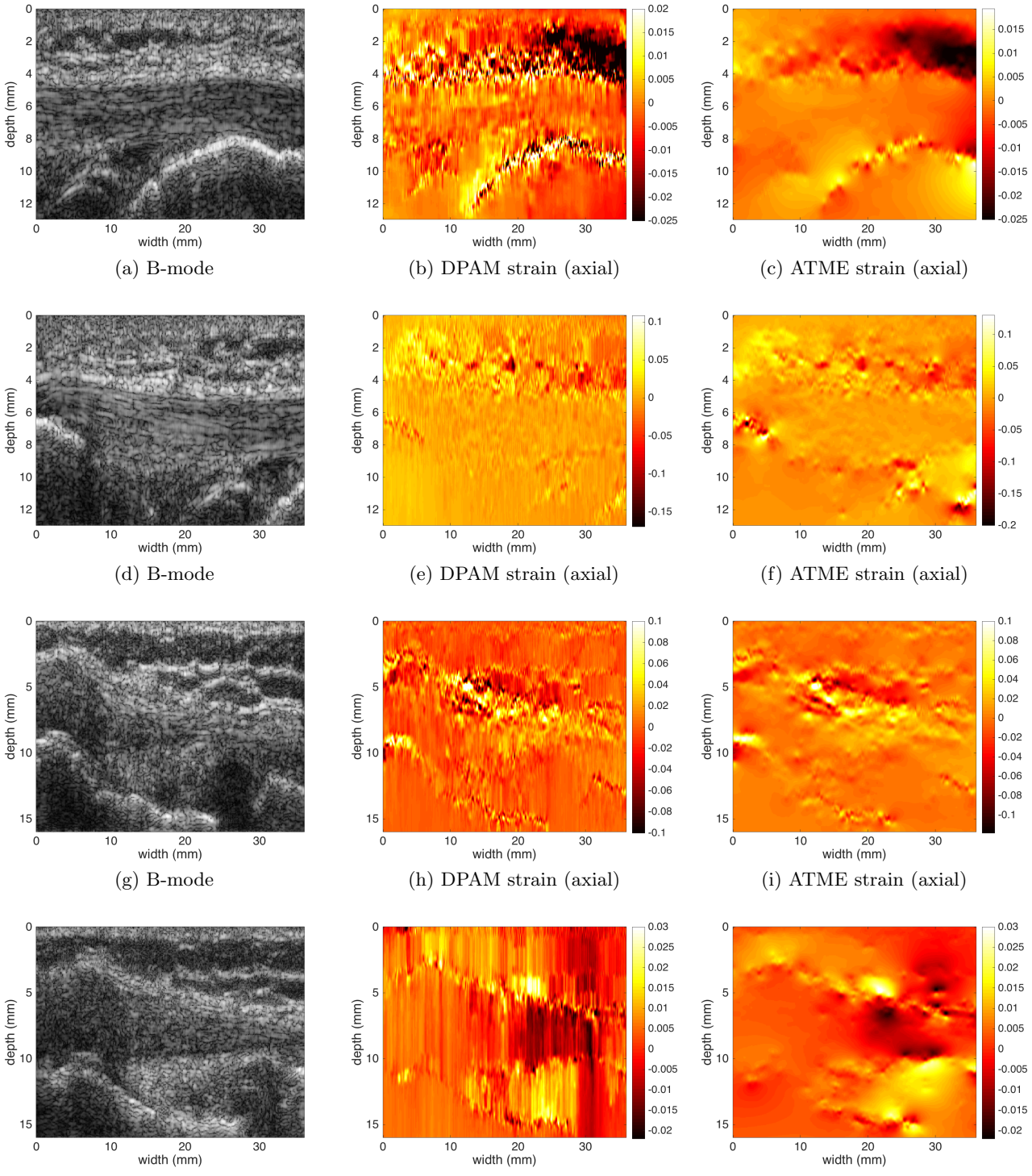

(a) B-mode (b) DPAM strain (axial) (c) ATME strain (axial)

(d) B-mode (e) DPAM strain (axial) (f) ATME strain (axial)

(g) B-mode (h) DPAM strain (axial) (i) ATME strain (axial)

(j) B-mode (k) DPAM strain (axial) (l) ATME strain (axial)

Figure 5: comparison between ATME and DPAM methods. (a), (b), and (c) show distal area of patellar tendon during force flexion experiment. (d), (e), and (f) are proximal region of patellar tendon. (g)-(l) are B-mode and strain images of MCL during pure valgus stress experiment.

[4] Zahiri-Azar, R. and Salcudean, S. E., "Motion estimation in ultrasound images using time domain cross correlation with prior estimates," *IEEE Transactions on Biomedical Engineering* **53**(10), 1990–2000 (2006).

[5] Treece, G., Lindop, J., Chen, L., Housden, J., Prager, R., and Gee, A., "Real-time quasi-static ultrasound elastography," *Interface focus* , rsfs20110011 (2011).

[6] Rivaz, H., Boctor, E., Foroughi, P., Zellars, R., Fichtinger, G., and Hager, G., "Ultrasound elastography: a dynamic programming approach," *IEEE transactions on medical imaging* **27**(10), 1373–1377 (2008).

[7] J Hall, T., E Barboneg, P., A Oberai, A., Jiang, J., Dord, J.-F., Goenezen, S., and G Fisher, T., "Recent results in nonlinear strain and modulus imaging," *Current medical imaging reviews* **7**(4), 313–327 (2011).

[8] Shams, R., Boily, M., Martineau, P. A., and Rivaz, H., "Dynamic programming on a tree for ultrasound elastography," in [*SPIE Medical Imaging*], 97901F–97901F, International Society for Optics and Photonics (2016).

[9] Rivaz, H., Boctor, E. M., Choti, M. A., and Hager, G. D., "Real-time regularized ultrasound elastography," *IEEE transactions on medical imaging* **30**(4), 928–945 (2011).

[10] Bergen, J. R., Anandan, P., Hanna, K. J., and Hingorani, R., "Hierarchical model-based motion estimation," in [*European conference on computer vision*], 237–252, Springer (1992).

[11] Jensen, J. A., "Field: A program for simulating ultrasound systems," in [*10th Nordicbaltic conference on biomedical imaging, vol. 4, supplement 1, part 1: 351–353*], Citeseer (1996).

[12] Chimenti, R. L., Flemister, A. S., Ketz, J., Bucklin, M., Buckley, M. R., and Richards, M. S., "Ultrasound strain mapping of achilles tendon compressive strain patterns during dorsiflexion," *Journal of biomechanics* **49**(1), 39–44 (2016).